Research paper

Identification of new potent A$_1$ adenosine receptor antagonists using a multistage virtual screening approach

Yu Wei [a,1], Mukuo Wang [a,1], Yang Li [a,1], Zhangyong Hong [b], Dongmei Li [a,**], Jianping Lin [a,c,d,*]

[a] State Key Laboratory of Medicinal Chemical Biology, College of Pharmacy and Tianjin Key Laboratory of Molecular Drug Research, Nankai University, Haihe Education Park, 38 Tongyan Road, Tianjin, 300353, China
[b] State Key Laboratory of Medicinal Chemical Biology, College of Life Sciences, Nankai University, 94 Weijin Road, Tianjin, 300071, China
[c] Biodesign Center, Tianjin Institute of Industrial Biotechnology, Chinese Academy of Sciences, 32 West 7th Avenue, Tianjin Airport Economic Area, Tianjin, 300308, China
[d] Platform of Pharmaceutical Intelligence, Tianjin International Joint Academy of Biomedicine, Tianjin, 300457, China

ABSTRACT

The use of antagonists for each adenosine receptor (AR) subtype as potent clinical candidates is of growing interest due to their involvement in the treatment of various diseases. The recent resolution of several A$_1$ and A$_{2A}$ ARs X-ray structures provides opportunities for structure-based drug design. In this study, we describe the discovery of novel A$_1$AR antagonists by applying a multistage virtual screening approach, which is based on random forest (RF), e-pharmacophore modeling and docking methods. A multistage virtual screening approach was applied to screen the ChemDiv library (1,492,362 compounds). Among the final hits, 22 compounds were selected for further radioligand binding assay analysis against human A$_1$AR, and 18 compounds (81.82% success) exhibited nanomolar or low micromolar binding potency (K_i). Then, we selected six compounds ($pK_i > 6$) to further evaluate their antagonist profile in a cAMP functional assay, and we found that they had low micromolar antagonistic activity ($pIC_{50} = 5.51-6.38$) for the A$_1$AR. Particularly, four of six compounds ($pK_i > 6$) showed very good affinity ($pK_i = 6.11-7.13$) and selectively (>100-fold) for A$_1$AR over A$_{2A}$AR. Moreover, the novelty analysis suggested that four of six compounds ($pK_i > 6$) were dissimilar to existing A$_1$AR antagonists and hence represented novel A$_1$AR antagonists. Further molecular docking and molecular dynamics (MD) studies showed that the three selective compounds 15, 20 and 22 were stabilized (RMS$_{lig}$ value $\leq$ 2 Å) inside the binding pocket of A$_1$AR with similar orientations to the docking pose in 100-ns MD simulations, whereas they escaped from the binding area of A$_{2A}$AR with larger values of RMS$_{lig}$ (RMS$_{lig} \geq$ 2 Å). We hope that these findings provide new insights into the discovery of drugs targeting A$_1$AR and facilitate research on new drugs and treatments for A$_1$AR-related human pathologies.

1. Introduction

Adenosine is an endogenous nucleoside that participates in a variety of human physiological effects via its specific receptors.

Adenosine receptors (ARs), as a family of membrane receptors, are members of the G protein-coupled receptor (GPCRs) superfamily [1]. To date, four different AR subtypes have been identified, A$_1$, A$_{2A}$, A$_{2B}$ and A$_3$ [2], which differ in their genomic structure and tissue distribution [3]. Due to their involvement in diverse biological effects through mediating the widespread signaling of the nucleoside adenosine, ARs have been considered potential drug targets in the treatment of various diseases, conditions and disorders [4,5]. For instance, activation of A$_1$ and A$_3$ ARs inhibits adenylyl cyclase activity, resulting in a decreased concentration of the 3′,5′-cyclic adenosine monophosphate (cAMP) and further inducing opening of potassium channels and indirectly reducing the penetration of

calcium into the cell [3]. In contrast, activation of A_{2A} and A_{2B} ARs stimulates adenylyl cyclase activity followed by an increased concentration of cAMP with an opposing effect [3]. The changes in adenosine levels are believed to closely correlate with certain kinds of physiopathological states such as psychosis and anxiety, neurodegenerative disorders, asthma and inflammatory diseases [6,7]. Moreover, selective agonists and antagonists are generally considered to be potential candidates in numerous therapeutic applications by modulating adenosine receptor-induced physiopathological processes.

Recently, many of the crystal structures obtained for A_{2A}AR bound to antagonists or agonists [8] and for A_1AR bound to selective antagonists [9,10] have contributed greatly to the characterization of adenosine receptor subtypes, facilitating our understanding of the structural basis for ligand recognition and providing insights into ways to develop high potential and selective AR modulators. The effective binding site of ARs ligands is similar across known AR subtypes, located in the upper region of the transmembrane (TM) bundle surrounded by TM3, 5, 6, and 7 [11]. For all four AR subtypes, mutagenesis data indicate that N(6.55) and L(6.51) are highly conserved residues and play an important role in the recognition of agonists and antagonists [12]. However, the extracellular sections of TM1, TM2 and TM7 in A_1AR are located far away from the core of the receptor, resulting in a slightly wider A_1AR binding pocket than A_{2A}AR. Moreover, the negatively charged E(5.30) in A_1 and A_{2A} ARs is substituted with valine in A_3AR, which allows the entry of ligands with lipophilic groups in this region of the A_3AR binding pocket. In particular, differences in ECL2 across the family of adenosine receptors play an important role in the ligand subtype selectivity between A_{2A}AR and A_{2B}AR and the agonist/antagonist binding affinity between A_1AR and A_3AR [9].

Among the four adenosine receptors, A_1AR was the first adenosine receptor identified by pharmacological analysis in 1979 [13] and was cloned from dog in 1991 [14]. A_1AR is widely expressed in the central nervous system and in peripheral tissue mediating protective effects against brain injury and ischemic kidney injury. In recent years, a large number of agonists and antagonists of A_1AR have been developed for the clinic; A_1AR antagonists have especially been demonstrated to provide outstanding outcomes in the regulation of, e.g., Alzheimer's disease (AD), cardiac disease and kidney disease [5,15,16]. 8-cyclopentyl-1,3-dipropylxanthine (DPCPX) was initially proposed as a highly potent A_1AR antagonist [17], while it also exhibited considerable affinity for A_{2A}AR and A_{2B}AR and weak affinity for A_3AR [5,18]. Rolofylline, an A_1AR antagonist, has been dropped from development as a drug for the regulation of heart and renal function in acute heart failure patients due to an increased rate of seizures and strokes [19,20]. Despite a large amount of research in the field of A_1AR antagonists, progress from abundant knowledge of A_1AR antagonist biology to clinical treatment has been slow. Therefore, an opportunity exists for further development of novel and potent A_1AR antagonists that avoid undesirable adverse events.

In recent years, many computer-aided drug design (CADD) techniques, such as ligand-based pharmacophore modeling [21–24], quantitative structure-affinity relationships (QSAR) [25–27], multilabel classification approach [28] and structure-based molecular docking [11,29–37], have been utilized in discovery of adenosine receptor ligands. Thus far, the development of A_1AR subtype ligands has focused on the independent application of ligand-based methods [22,28] and structure-based homology modeling based on the crystal structure of A_{2A}AR serving as a template [32,34]. For instance, Kolb et al. built multiple homology models for A_1AR and docked two million compounds, finally obtaining numerous potent and novel ligands with a highest affinity of 400 nM [34]. In 2012, Horst et al. developed a

pharmacophore model for A_1AR and obtained a compound with moderate affinity for A_1AR but negligible affinity for the A_{2A}AR, A_{2B}AR and A_3AR subtypes [22]. Moreover, as a computational chemogenomic approach, proteochemometric (PCM) modeling takes the protein-compound cross-terms into account to construct a predictive model and explore protein-compound interactions for multiple target proteins and protein families [38]. By combining human and rat bioactivity data, van Westen et al. utilized PCM to rapid virtual screening of novel small molecule ligands for A_1AR, A_{2A}AR, A_{2B}AR and A_3AR, and they identified six novel compounds by "wet" experimental validation [39]. However, there has been a lack of investigations to identify A_1AR subtype ligands using the multistage virtual screening (VS) approach combining ligand-based and structure-based strategies, which has been successfully applied in new lead compound identification in many studies [40,41].

In this study, we focused on the identification of highly active A_1AR ligands using a multistage virtual screening strategy combining random forest (RF), e-pharmacophore and protein-ligand molecular docking methods. Screening of the ChemDiv library (1,492,362 compounds) resulted in the identification of 18 of 22 selected and experimentally tested compounds as positive hits; six of 18 hits were identified as new high-affinity hits with nanomolar level binding affinity for the A_1AR, and four of six high potent hits were found to be highly selective (>100-fold) for A_1AR over A_{2A}AR. Molecular dynamics simulation was performed to further explore the affinity and selectivity of compounds at the A_1 and A_{2A} ARs.

2. Results and discussion

A schematic workflow of the multistage virtual screening methods is presented in Fig. 1.

2.1. Construction and validation of the RF model

RF, as a classification technique based on ensembles of multiple decision trees and a majority-voting scheme, has been widely used in drug discovery for drug toxicity prediction [42], bioactivity classification [43], drug target identification [44], and protein-ligand affinity prediction [45], among other uses. Svetnik et al.
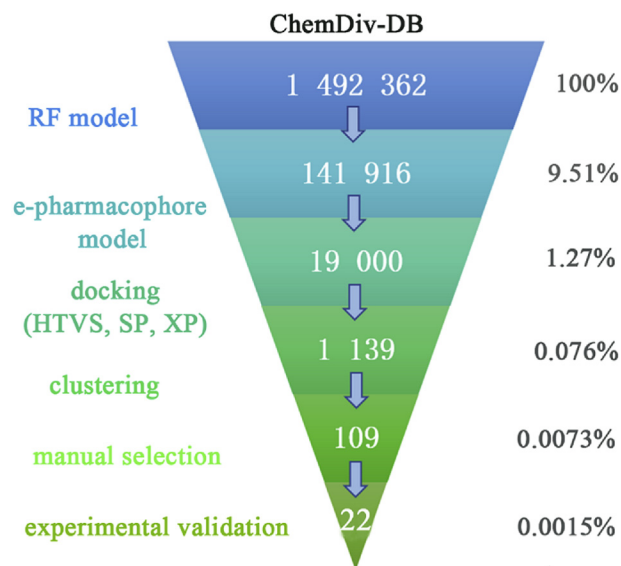

Fig. 1. Workflow of the multistage virtual screening of the ChemDiv library targeting A_1AR.

[46] demonstrated that the accuracy of RF is comparable to the that of the support vector machine (SVM) and neural networks, and the RF possesses the characteristic of superior interpretability. Ruano-Ordás et al. [47] suggested that the RF, which is an ensemble learning method by the combination of classifiers, could achieve excellent performance in the case of complicated datasets (unbalanced nature, dimensionality and hidden dependences).

For the generation of RF classification models for A_1AR antagonists, we employed three training sets to train the RF models. The three training sets comprised 80% of the K-200 dataset (1112 known active molecules at A_1AR ($K_i < 100$ nM) and 1998 inactive molecules at A_1AR ($K_i > 200$ nM)), K-1000 dataset (1112 known active molecules at A_1AR ($K_i < 100$ nM) and 997 inactive molecules at A_1AR ($K_i > 1000$ nM)) and K-2000 dataset (449 active molecules at A_1AR ($K_i < 20$ nM) and 623 inactive molecules at A_1AR ($K_i > 2000$ nM)), respectively. Initially, thousands of descriptors for the compounds in each dataset (K-200, K-1000 and K-2000) were calculated using Dragon 6.0. The correlation coefficients between all pairs of descriptors were analyzed to identify redundant descriptors. One of descriptors with a correlation coefficient higher than 95% was then removed. Moreover, descriptors that had too many zero values, or standard deviation values < 0.5%, were discarded to achieve a smaller data set. As a result, the number of descriptors used for the K-200, K-1000 and K-2000 datasets was 549, 547 and 484, respectively. Subsequently, three full RF models were built for the K-200, K-1000 and K-2000 datasets using training sets with all available descriptors, after which the test sets (20% of K-200, K-1000 and K-2000 datasets, respectively) were used to evaluate the performance of the models.

The test set results for K-200, K-1000 and K-2000 are presented in Table 1. Many metrics are used to evaluate the performance of the different RF models, for instance, the sensitivity (SE), specificity (SP), overall accuracy (Q), Matthews correlation coefficient (MCC) and area under the receiver operating characteristic curve (AUC). Table 1 shows that the RF model (M-200I) was built based on the K-200 dataset with SE of 67%, SP of 92.9%, Q of 83.7%, MCC of 0.64 and AUC of 0.90, the RF model (M-1000I) was based on the K-1000 dataset with SE of 88.6%, SP of 81.8%, Q of 85.4%, MCC of 0.71 and AUC of 0.93, and the RF model (M-2000I) was based on the K-2000 with SE of 90.0%, SP of 88.7%, Q of 89.3%, MCC of 0.79 and AUC of 0.96. It should be noted that the SE and SP values of the M-2000I model were higher than those of the M-200I and M-1000I models, indicating higher prediction accuracies for activities and inactivities. The M-2000I model achieving a maximum MCC of 0.79 with 0.96 AUC and 89.3% overall accuracy indicated that the overall prediction accuracy of M-2000I was better than those of M-200I and M-1000I. The predictive performance of the RF model

generated from the K-2000 dataset was better than that of the RF models constructed from K-200 and K-1000. The cut-off value (activity defined as $K_i < 20$ nM and inactivity defined as $K_i > 2000$ nM) providing the best performance for the RF model (M-2000I) was used, and the M-2000I model was accordingly adopted for further investigation of the compound classification.

In the first stage, a full RF model (M-2000I) was built using all 484 available descriptors. Subsequently, the importance of the descriptors used in the M-2000 model was estimated by the RF algorithm by calculating the mean decrease in the Gini index (MeanDecreaseGini) for each descriptor. The MeanDecreaseGini measure was used to drop unimportant descriptors from the M-2000I model. In the second stage, after discarding the less important descriptors (MeanDecreaseGini < 2), a total of 31 descriptors were retained and used to build a second RF model (M-2000II). In the third stage, the descriptors with MeanDecreaseGini >14 were retained to build a third RF model (M-2000III). Generally, 10-fold internal cross-validation or 5-fold external validation [48] is used to assess the performance of machine learning models. The evaluation results of three RF models (M-2000I, M-2000II, and M-2000III) by applying out-of-bag (OOB) validation and 10-fold internal cross-validation, which is performed using the KNIME program [49], are presented in Table S1. The results shown in Table S1 indicate that M-2000II and M-2000III produce the high SE, SP, Q and MCC in the OOB validation as well as in the 10-fold cross-validation, compared with M-2000I.

Furthermore, the performance of three RF models (M-2000I, M-2000II, and M-2000III) evaluated using an external test set from the K-2000 dataset is shown in Table 2. M-2000II achieves a maximum MCC of 0.81 with 90.6% overall accuracy, indicating that the overall prediction accuracy of M-2000II is better than those of M-2000I and M-2000III. Compared with model M-2000I, M-2000II has better performance with fewer descriptors but higher accuracy. With a continued decrease in the number of descriptors, M-2000III suffers a decline in performance with reduced SE, SP, Q and MCC values. Finally, RF model M-2000II was adopted for further research in virtual screening of the compound database.

2.2. E-pharmacophore model generation and validation

The Glide XP energetic terms calculated using structural and energy information between the PSB36 and A_1AR were mapped onto pharmacophore sites to develop the pharmacophore hypothesis. The root-mean- square deviation (RMSD) value between the redocked and crystal conformation of PSB36 was 1.9 Å. The pharmacophore features with an energetic value < −0.5 kcal/mol were retained and used to compose the pharmacophore

Table 1
The test results for the RF models constructed based on the K-200, K-1000 and K-2000 datasets.

Model	Number of descriptors	TP[a]	FP[b]	TN[c]	FN[d]	SE (%)[e]	SP (%)[f]	Q (%)[g]	MCC[h]	AUC[i]
M-200I	549	148	28	369	73	67.0	92.9	83.7	0.64	0.90
M-1000I	547	195	36	162	25	88.6	81.8	85.4	0.71	0.93
M-2000I	484	90	14	110	10	90.0	88.7	89.3	0.79	0.96

[a] TP: true positive.
[b] FP: false positive.
[c] TN: true negative.
[d] FN: false negative.
[e] SE (%): sensitivity, SE = TP/(TP + FN).
[f] SP (%): sepecificity, SP = TN/(TN + FP).
[g] Q (%): overall accuracy, Q = (TP + TN)/(TP + FP + TN + FN).

[h] MCC: $MCC = \dfrac{TP \times TN - FN \times FP}{\sqrt{(TP+FN)(TP+FP)(TN+FN)(TN+FP)}}$.

[i] AUC: the area under the receiver operating characteristic curve.

Table 2
The test results for three RF models constructed based on the K-2000 dataset using different descriptors.

Model	Number of descriptors	TP	FP	TN	FN	SE(%)	SP(%)	Q(%)	MCC	AUC
M-2000I	484	90	14	110	10	90.0	88.7	89.3	0.79	0.96
M-2000II	31	91	12	112	9	91.0	90.3	90.6	0.81	0.95
M-2000III	16	87	14	110	13	87.0	88.7	87.9	0.76	0.95

hypothesis. An e-pharmacophore hypothesis was then generated comprising a hydrogen bond acceptor (A3), two hydrogen bond donors (D4 and D5), one hydrophobic group (H11) and one aromatic ring (R12) (Fig. 2). The energy value for favorable features in the hypothesis is A3 of −2.14 kcal/mol, D4 of −1.10 kcal/mol, D5 of −2.14 kcal/mol, H11 of −0.55 kcal/mol and R12 of −1.04 kcal/mol. The higher absolute value of the feature energy indicates that ligand atom mapping exhibits more potent interaction energy with amino acids.

In an effort to evaluate the performance of the e-pharmacophore hypothesis (A3D4D5H11R12), a validation set (37 known A_1AR antagonists and 1332 decoys) was used to explore the ability of the e-pharmacophore hypothesis to differentiate the antagonists from the decoys. Screening molecules in the validation set were required to match a minimum of two - four sites for the hypotheses. The validation results of the e-pharmacophore hypothesis are presented in Table 3. The enrichment factor in the top 1% of compounds screened (EF1%) and Boltzmann-enhanced discrimination of the receiver operating characteristic (BEDROC) [50] are used to assess the number of known antagonists recovered in virtual screening and the early scoring problem, respectively. The value of $\alpha = 160.9$ in BEDROC refers to 80% of the total score derived from the top 1% of the database, whereas the value of $\alpha = 20.0$ refers to 80% of the total score derived from the top 8% of the database. Moreover, the AUC and the area under the accumulation curve (AUAC) were employed to evaluate the performance of the e-

Table 3
EF1%, BEDROC at $\alpha = 160.9$ and 20, AUC, AUAC and ranked actives of the screened validation set.

Matches	EF1%	BEDROC $\alpha = 160.9$	BEDROC $\alpha = 20.0$	AUC	AUAC	Ranked Actives
2 of 5	13.69	0.44	0.22	0.47	0.60	20
3 of 5	13.69	0.44	0.22	0.47	0.60	20
4 of 5	13.69	0.50	0.42	0.75	0.80	31

pharmacophore hypothesis. Table 3 shows that the e-pharmacophore hypothesis with a minimum of four sites used for screening outperform those with a minimum of two - three sites, corresponding to the EF1% of 13.69, BEDROC ($\alpha = 160.9$) of 0.50, BEDROC ($\alpha = 20.0$) of 0.42, AUC of 0.75 and AUAC of 0.80. Accordingly, 31 of 37 known antagonists were retrieved from validation set, making the hypothesis with a minimum of four matched sites more practical for screening. Six known antagonists that were not retrieved from the validation set are shown in Fig. S1. Finally, the e-pharmacophore hypothesis (A3D4D5H11R12) was further utilized during virtual screening of the database.

2.3. Virtual screening

To evaluate the molecular docking accuracy, PSB36 was extracted from the cocrystallized PDB complex (PDB ID 5N2S) and redocked into the A_1AR crystal structure 5N2S using three docking protocols including high-throughput virtual screening (HTVS), standard precision (SP) and extra precision (XP). Default docking parameters were used. The RMSD values between the redocked and crystallized conformations are listed in Table S2. The RMSD values produced by three docking protocols are less than 2 Å, indicating that Glide HTVS, SP and XP are reliable methods for docking study in this study.

Based on our previous observation, a multistage method that sequentially applied the RF model, e-pharmacophore models and docking protocols taking into account the efficiency and effectiveness is practical [51]. Therefore, the RF model, e-pharmacophore models and docking protocols were used in sequence to filter a ChemDiv library containing 1,492,362 compounds to retrieve novel and potent A_1AR antagonists (Fig. 1). First, the RF model M-2000II with 31 descriptors was used to filter the entire ChemDiv library, resulting in a total of 141,916 compounds that passed the screening. Second, these 141,916 compounds were further screened by the e-pharmacophore model, and 19,000 compounds remained. Third, these 19,000 compounds were used for molecular docking screening using Glide HTVS, SP and XP functions in the Virtual Screening Workflow. Then, a total of 1,139 compounds were obtained from the docking. To explore the chemotype diversity, these 1,139 compounds were classified into 109 clusters according to their molecular structures using spectral clustering. The potency of the compounds in each cluster were further assessed by visual inspection of their interactions with amino residues in the orthosteric ligand binding pocket of A_1AR. Finally, a total of 22 compounds were selected for further in vitro validation of bioactivity against A_1AR.
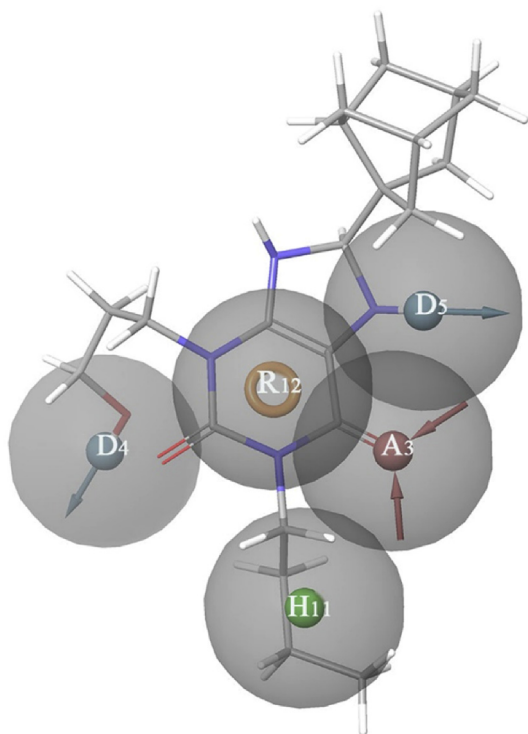

Fig. 2. E-pharmacophore hypothesis with energetically favorable sites from the cocrystal structure (PDB ID 5N2S).

2.4. Biological evaluation

2.4.1. A_1/A_{2A} ARs affinity and selectivity experiments

Table 4 summarizes the obtained binding affinities of selected compounds from multistage virtual screening in radioligand binding assays at human A_1 and A_{2A} ARs. For comparison, the A_1 adenosine receptor antagonist DPCPX and $A_{2A}AR$ antagonist ZM241385 are also provided in Table 4.

Initially, all 22 compounds (No. 1−22) were screened at an initial concentration of 100 μM in 3-fold serial dilutions with A_1AR. For compounds that inhibited radioligand binding by more than 50% at A_1AR, K_i values were subsequently determined (Table 4). As summarized in Table 4, 18 of 22 compounds ("hit rate" of 81.82%) showed activity toward A_1AR. Six compounds ($pK_i > 6$) had nanomolar affinity for A_1AR, and twelve compounds ($pK_i > 4.49$) had micromolar affinity for A_1AR.

For those six compounds (No. 12, 15, 16, 19, 20 and 22) with nanomolar affinity ($pK_i > 6$) at A_1AR, the selectivity for A_1AR over $A_{2A}AR$ was further investigated. The concentration-response curves of six compounds against A_1 and A_{2A} ARs in the radioligand binding assay are presented in Fig. S2 − S3. As shown in Table 4, six compounds exhibited different degrees of affinity and selectivity toward the A_1 and A_{2A} ARs. Among them, three compounds (No. 16, 20 and 22) exhibited ~100 times more binding affinity for A_1AR ($pK_i = 6.15$ for compound 16, $pK_i = 6.11$ for compound 20, $pK_i = 6.29$ for compound 22) in comparison to $A_{2A}AR$ ($pK_i < 4$). Similarly, compound 19 was ~100 times more selective for the A_1AR ($pK_i = 6.68$) than the $A_{2A}AR$ ($pK_i = 4.42$). Moreover, compound 15 was found to possess ~1000 times more binding affinity for A_1AR ($pK_i = 7.13$) than $A_{2A}AR$ ($pK_i < 4$). However, compounds 12 was ~60 times more potent at A_1AR ($pK_i = 6.23$) compared with $A_{2A}AR$ ($pK_i = 4.44$).

2.4.2. Functional experiments

Compounds 12, 15, 16, 19, 20 and 22, the most potent in terms of A_1AR affinity, were further analyzed to evaluate their A_1AR antagonistic effect. The assay was then carried out to evaluate the effect of these compounds on NECA-mediated cAMP inhibition in human A_1AR CHO cells. Concentration-response curves of six compounds against the A_1AR in the cAMP assay are presented in Fig. S4. The results showed that all six compounds were able to counteract the inhibitory effect of the A_1AR agonist NECA on cAMP production with low micromolar antagonistic activity ($pIC_{50} = 5.51–6.38$). Compounds 12, 15, 16, 19, 20 and 22 with pK_i of 6.23, 7.13, 6.15, 6.68, 6.11 and 6.29 in the binding affinity assay showed pIC_{50} of 5.55, 6.38, 5.90, 5.73, 5.83 and 5.51 in the cAMP functional assay, respectively. Five of those compounds (No. 12, 16, 19, 20 and 22) displayed pIC_{50} values in the micromolar range (pIC_{50} of 5.51–5.90), corresponding to their pK_i values ranging from 6 to 7. Among all compounds, compound 15 possessed the most antagonist activity with an pIC_{50} of 6.38, which is in accordance with the significant binding affinity value ($pK_i = 7.13$) obtained in the radioligand binding assay. It is noteworthy that the pIC_{50} values presented a similar trend to the binding affinity data. Compound 15 was the most potent A_1AR antagonist ($pIC_{50} = 6.38$).

2.5. Novelty analysis of hit compounds

To further investigate the novelty of the tested compounds, the pairwise similarity between the tested compounds and all the known A_1AR ligands in the ChEMBL 24 was calculated based on the extended connectivity fingerprints (ECFPs) using the Schrödinger Canvas program [52,53]. The Tanimoto coefficients (Tc), ranging from 0 (complete dissimilarity) to 1 (identical), was employed to compare the chemical similarity between two molecules. For each

of six hits (compounds 12, 15, 16, 19, 20 and 22), the maximum Tc values compared to all of the known A_1AR ligands in the ChEMBL 24 are presented in Table 4. A pair of molecules with chemical dissimilarity have a low Tc value close to 0, whereas identical pairs possess a Tc value equal to 1. The results in Table 4 show that the Tc values of six hits ranged from 0.29 to 0.64. Compound 15 and compound 19 had pK_i values of 7.13 and 6.68, respectively, and Tc values greater than 0.6. These compounds are derivatives of 2-amino nicotinonitrile, a nonxanthine type of previously known AR antagonists with high affinity [54]. It is interesting, however, that compounds 12, 16, 20 and 22 were found to be potent antagonists of A_1AR with pK_i values ranging from 6.11 to 6.29 and pIC_{50} values ranging from 5.51 to 5.90, whereas the Tc values of these hits were all less than 0.4. Hence, the novel chemotypes identified from multistage virtual screening were reflected by their low Tc values and are expected to be promising candidates for A_1AR.

2.6. Molecular modeling exploration

To explore the affinity and selectivity of compounds on A_1 and A_{2A} ARs, molecular docking and molecular dynamic simulation were performed.

PSB36 is selective for A_1AR ($pK_i = 9.16$), and its affinity for $A_{2A}AR$ is submicromolar. ZM241385 is the $A_{2A}AR$-selective antagonist ($pK_i = 9.52$) over A_1AR ($pK_i = 5.69$) [56]. We chose PSB36 and ZM241385 as control molecules to explore the mechanism responsible for the selectivity between A_1AR and $A_{2A}AR$ of compound 15, 20 and 22. In our docking studies, PSB36 had a similar docking pose against A_1AR and $A_{2A}AR$, providing the same result as ZM241385 and compound 15 against these two receptors, respectively (Fig. S5A, S5B and S5C). The predicted binding energy in the docking studies for PSB36 was stronger against A_1AR (−11.51 kcal/mol) than against $A_{2A}AR$ (−10.33 kcal/mol). ZM241385 had a stronger predicted binding energy against $A_{2A}AR$ (−11.05 kcal/mol) than against A_1AR (−7.36 kcal/mol). This result is consistent with the selectivity of PSB36 and ZM241385 between the two receptors. The binding energy of compound 15 was −11.72 and −9.95 kcal/mol against A_1AR and $A_{2A}AR$, which implied that compound 15 possessed a stronger affinity for A_1AR. Compound 20 and 22 had two binding orientations with very close binding energies against $A_{2A}AR$ (Fig. S6); herein we adopted both binding orientations to perform the MD simulations. The two orientations are referred to as compound-20A (compound-22A) and compound-20B (compound-22B). Compound-20B and compound-22B had a similar docking pose against $A_{2A}AR$ as against A_1AR (Figs. S6B and S6D). The binding energies of compounds 20 and 22 were smaller against A_1AR than $A_{2A}AR$, which implied that compounds 20 and 22 also had a stronger affinity for A_1AR than $A_{2A}AR$. The predicted binding energy for PSB36, ZM241385, compound 15, 20 and 22 (including compound-20 A and 20B and compound-22A and 22B) are presented in Table S3.

Additionally, the docking poses of five ligands inside the orthosteric binding site of A_1AR and $A_{2A}AR$ were used as starting structures to perform MD simulations. The 100-ns MD simulations were performed for the 12 systems of PSB36, ZM241385 and compound 15 and 20 (compound-20A, 20B and 22 (compound-22A and 22B)) combined with A_1AR and $A_{2A}AR$. Each system was embedded in hydrated POPE bilayers. The RMSD measures during the last 5-ns MD trajectory (including RMS$_{prot}$ (which is the protein backbone RMSD with respect to the minimized structure) and RMS$_{lig}$ (which is the RMSD of the ligand inside the binding site with respect to its docking pose coordinates)) of the 12 simulated systems are shown in Table 5. The RMS$_{prot}$ values ranged from 1.88 to 2.65 Å with standard deviations of approximately 0.2 Å, suggesting that the systems achieved stability and were equilibrated during

Table 4
Binding affinities (pK$_i$) obtained from radioligand binding assays at human A$_1$ and A$_{2A}$ ARs, potencies (pIC$_{50}$) at human A$_1$AR and chemical structures of 22 hits (compounds 1−22) from multistage virtual screening.
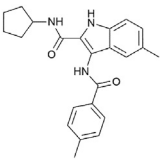
Compound number	Compound ID	Chemical structures	Binding affinities pK$_i$[a]		SI[b] (A$_1$/A$_{2A}$)	cAMP assays pIC$_{50}$	Tc
			A$_1$	A$_{2A}$	A$_1$/A$_{2A}$		
1	7365−0104		4.70	−[c]	−	−	−
2	5228−4343		4.73	−	−	−	−
3	D481-0619		4.49	−	−	−	−
4	8020−4802		5.52	−	−	−	−
5	G856-0916		ND[d]	−	−	−	−
6	3535−0081		5.16	−	−	−	−
7	4428−0413		4.87	−	−	−	−
8	5742−0670		4.59	−	−	−	−
9	8407−0221		5.49	−	−	−	−
10	J023-0328		5.14	−	−	−	−
11	K788-4209		5.95	−	−	−	−

Table 4 (continued)

Compound number	Compound ID	Chemical structures	Binding affinities pK$_i$[a]		SI[b] (A$_1$/A$_{2A}$)	cAMP assays pIC$_{50}$	Tc
			A$_1$	A$_{2A}$	A$_1$/A$_{2A}$		
12	L935-0357		6.23	4.44	0.016	5.55	0.34
13	0160−0864		ND	−	−	−	−
14	8020−0248		ND	−	−	−	−
15	3829−0650		7.13	<4	<0.001	6.38	0.60
16	G856-1381		6.15	<4	<0.01	5.90	0.32
17	6855−0017		ND	−	−	−	−
18	D481-1775		4.97	−	−	−	−
19	3483−0350		6.68	4.42	0.006	5.73	0.64
20	D718-0907		6.11	<4	<0.01	5.83	0.29
21	C620-0253		4.71	−	−	−	−

Table 4 (*continued*)

Compound number	Compound ID	Chemical structures	Binding affinities pK$_i$[a]		SI[b] (A$_1$/A$_{2A}$)	cAMP assays pIC$_{50}$	Tc
			A$_1$	A$_{2A}$	A$_1$/A$_{2A}$		
22	L881-0032		6.29	<4	<0.01	5.51	0.32
	DPCPX		0.002	0.13[e]			
	ZM241385		0.54[e]	0.004			

[a] All pK$_i$ values were determined in duplicate assay.
[b] The selectivity index (SI) was calculated as the K$_i$ (A$_1$)/K$_i$ (A$_{2A}$) ratio.
[c] Biological assays were not performed.
[d] Binding affinity values at A$_1$AR were not determined.
[e] Ref. [55].

Table 5
RMS$_{prot}$ and RMS$_{lig}$ of PSB36, ZM241385, compound 15, 20 and 22 against A$_1$AR and A$_{2A}$AR based on the last 5-ns MD trajectory.

	A$_1$AR				A$_{2A}$AR			
	RMS$_{prot}$	SD	RMS$_{lig}$	SD	RMS$_{prot}$	SD	RMS$_{lig}$	SD
PSB36	2.01	0.15	1.74	0.16	2.30	0.20	2.53	0.20
ZM241385	2.65	0.25	4.24	0.18	2.18	0.15	1.80	0.31
Compound 15	1.95	0.12	1.92	0.23	2.56	0.14	3.81	0.51
Compound 20	2.35	0.10	1.34	022	1.88[a]/1.95[b]	0.15[a]/0.12[b]	4.75[a]/4.33[b]	0.64[a]/0.75[b]
Compound 22	2.24	0.11	1.59	0.24	1.98[a]/1.96[b]	0.11[a]/0.14[b]	3.06[a]/5.86[b]	0.55[a]/0.14[b]

[a] The RMS$_{prot}$ and RMS$_{lig}$ of compound-20A (compound-22A).
[b] The RMS$_{prot}$ and RMS$_{lig}$ of compound-20B (compound-22B).

the last 5-ns MD trajectory. For the control systems, the RMS$_{lig}$ of the PSB36-A$_1$ and A$_{2A}$ ARs, ZM241385-A$_1$ and A$_{2A}$ ARs complexes were 1.74 Å, 2.53 Å, 4.24 Å, and 1.80 Å, respectively. Additionally, the ligands maintained a binding orientation similar to the docking pose (Figs. S7A and S7D), while they escaped from the binding area in the 100-ns MD simulations for the PSB36-A$_{2A}$AR and ZMA241385-A$_1$AR complexes (Figs. S7B and S7C). Since a larger RMS$_{lig}$ value (RMS$_{lig}$ value $\geq$ 2 Å) indicates that the ligand is unstable in or even escapes from the orthosteric binding area, the lower binding affinity correlates with a larger RMS$_{lig}$. Therefore, the smaller RMS$_{lig}$ values (RMS$_{lig}$ value $\leq$ 2 Å) of PSB36-A$_1$AR and ZM241385-A$_{2A}$AR indicate A$_1$AR subtype selectivity of PSB36 and A$_{2A}$AR subtype selectivity of ZM241385.

Similarly, the 100-ns MD simulations showed that compound 15, 20 and 22 were stabilized inside the binding pocket of A$_1$AR with a similar orientation to the docking pose (Table 5, Figs. 3A, 4A and 5A), resulting in good affinity against A$_1$AR (pK$_i$ = 7.13, 6.11, and 6.29, respectively). In the compound 15-A$_1$AR complex, the 6-amino group and nitrogen of the pyridine ring were hydrogen bonded to the side chain carbonyl and amino group of Asn254[6.55], respectively. The benzene group of the 1.3-benzodioxolan and pyridine rings formed the π-π stacking interaction with Phe171[ECL2]. Additionally, the ligand extended deeper into the orthosteric binding area and formed van der Waals interactions with residues Val62[2.57], Ile69[2.64], and Val87[3.32]. These interactions were maintained from the origin to the end of the 100-ns simulation (Fig. 3A) and the RMS$_{lig}$ value of 1.92 Å for the compound 15-A$_1$AR complex (Table 5). As revealed by mutagenesis experiments, Asn254[6.55] and Phe171[ECL2] can play important roles in both antagonist and agonist binding. In the compound 15-A$_{2A}$AR complex by comparison, compound-15 had a large RMS$_{lig}$ value of 3.81 Å and moved outward to the cytoplasm with respect to the structure at the beginning of the MD simulation, forming a hydrogen bond with Glu169[ECL2]. The ligand formed a π-π stacking interaction with Phe168[ECL2] through the benzene group of the 1.3-benzodioxolan part, but it could no longer form a hydrogen bond with Asn253[6.55] in its docking pose at the end of the simulation (Fig. 3B). We further calculated the binding free energy using the MM-PBSA method based on the last 5-ns MD trajectory. The total binding free energy was higher for compound 15-A$_{2A}$AR than compound 15-A$_1$AR (Table S4). The results from the MD simulation implied that compound 15 showed stronger affinity against A$_1$AR than A$_{2A}$AR. For compound 15-A$_{2A}$AR, compound 15 escaped from the binding area and was devoid of biological potency due to the absence of important attractive interactions.

For the compound 20-A$_1$AR complex, the carbonyl group and nitrogen N$_3$ of the pyrido[2,3-d]pyrimidin-4-one ring were hydrogen bonded to the side chain amino and carbonyl group of Asn254[6.55], respectively. The pyrido[2,3-d]pyrimidin-4-one ring formed the π-π stacking interaction with Phe171[ECL2], and the 4-chlorophenyl of compound 20 formed van der Waals interactions with residues Val87[3.32], Leu88[3.33], Met180[5.38] and Trp247[6.48]. These interactions were maintained during the 100-ns simulation (Fig. 4A). The conformation for compound 20 slightly changed with the RMS$_{lig}$ value of 1.34 Å for the compound 15-A$_1$AR complex (Table 5). For compound-20A and compound-20B, representing two modes against A$_{2A}$AR, the conformation for compound 20 showed a larger change with an RMS$_{lig}$ value of 4.75 and 4.33 Å for compound-20A and compound-20B. As shown in Fig. 4B and C, compound-20A moved outward to the cytoplasm with respect to the docking pose, forming a hydrogen bond with Glu169[ECL2] and only one hydrogen bond with Asn253[6.55]. Compound-20A lost the π-π stacking interaction Phe168[ECL2] with respect to its docking pose. Compound-20B also greatly changed and was unable to contact both Glu169[ECL2] and Asn253[6.55] with respect to the docking pose at the end of the simulation (Fig. 4B and C). The calculated
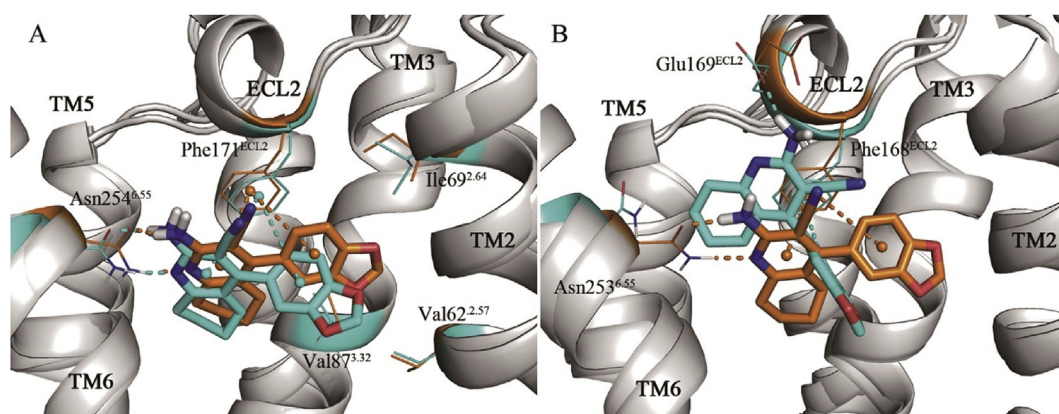
Fig. 3. (A) Superposition of compound 15 in the orthosteric binding area of A_1AR at the beginning (in yellow color for sticks, dots and lines) and last MD trajectory (in cyan). (B) Superposition of compound 15 in the orthosteric binding area of $A_{2A}AR$ at the beginning (in yellow) and last MD trajectory (in cyan). The protein is shown as a white cartoon. The hydrogen bonds between compound 15 and A_1AR are represented by dashed lines. The side chains of Phe171^{ECL2} and Asn254$^{6.55}$ (Phe168^{ECL2} and Asn253$^{6.55}$ in $A_{2A}AR$) are represented by sticks. The centers of the phenyl group of Phe171^{ECL2} (Phe168^{ECL2}) and the benzene group of the 1.3-benzodioxolan ring and pyridine ring of compound 15 are indicated by dots, and the π-tacking is represented by dashed lines. (For interpretation of the references to color in this figure legend, the reader is referred to the Web version of this article.)
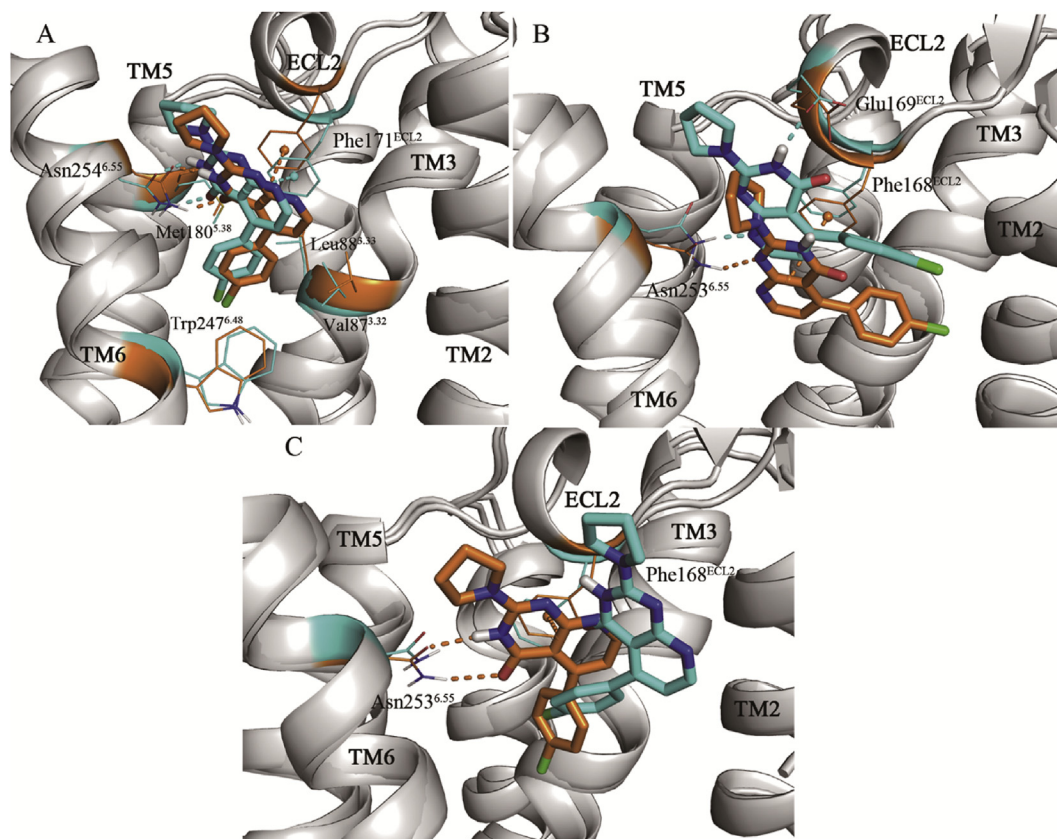
Fig. 4. (A) Superposition of compound 20 in the orthosteric binding area of A_1AR at the beginning (in yellow color for sticks, dots and lines) and last MD trajectory (in cyan). (B) Superposition of compound-20A against $A_{2A}AR$ (in compound-20A binding mode) at the beginning (in yellow) and last MD trajectory (in cyan). (C) Superposition of compound-20B against $A_{2A}AR$ at the beginning (in yellow) and last MD trajectory (in cyan). The protein is shown as a white cartoon. The hydrogen bonds between compound 20 and ARs are represented by dashed lines. The side chains of Phe171^{ECL2} and Asn254$^{6.55}$ (Phe168^{ECL2}, Glu169^{ECL2} and Asn253$^{6.55}$ in $A_{2A}AR$) are represented by sticks. The centers of the phenyl group of Phe171^{ECL2} (Phe168^{ECL2}) and the pyrido[2,3-d]pyrimidin-4-one ring of compound 20 are indicated by dots, and the π-tacking is represented by dashed lines. (For interpretation of the references to color in this figure legend, the reader is referred to the Web version of this article.)

binding free energies based on the last 5-ns MD for compound-20A and 20B were −27.63 and −24.17 kcal/mol, respectively. Compound 20-A_1AR showed a lower value of −42.95 kcal/mol (Table S4). The total binding free energy was lower for compound 20-A_1AR than compound 20-$A_{2A}AR$, consistent with the experimental observation that compound 20 showed a higher binding affinity against A_1AR than against $A_{2A}AR$.

In the compound 22-A_1AR complex, compound 22 formed two hydrogen bonds with the side chain of Asn254$^{6.55}$. The indole ring formed the π-π stacking interaction with the side chain of
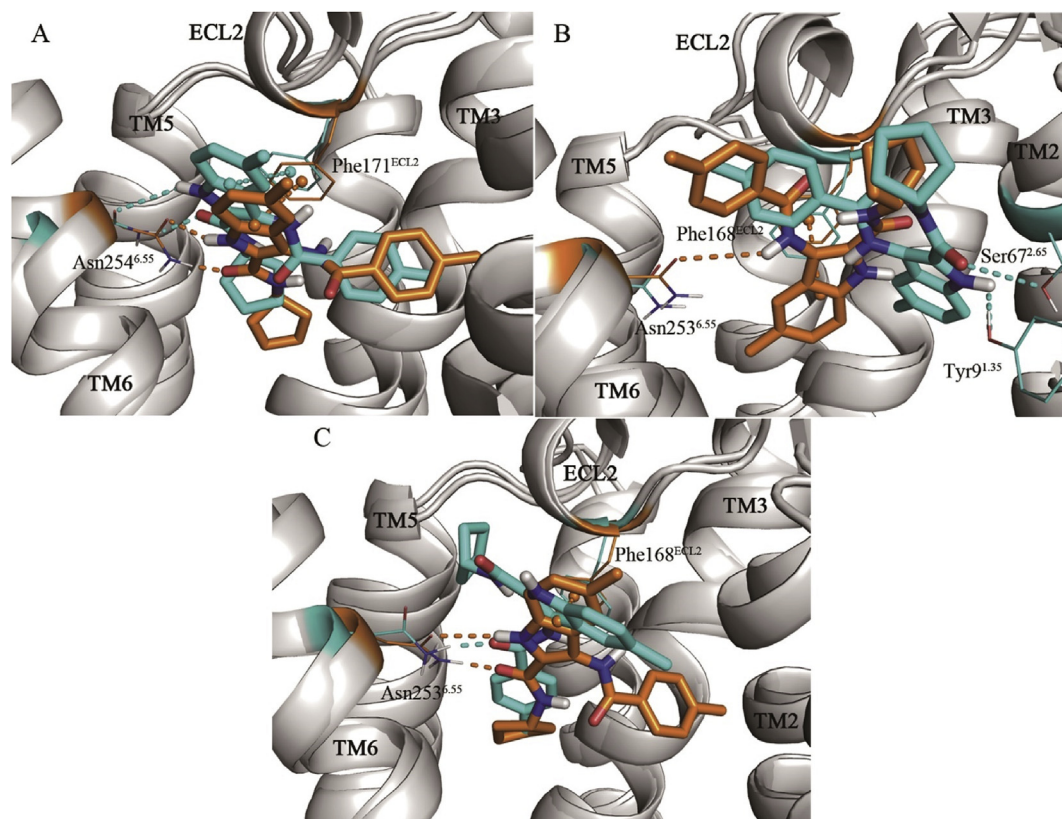
Fig. 5. (A) Superposition of compound 22 in the orthosteric binding area of A_1AR at the beginning (in yellow color for sticks, dots and lines) and last MD trajectory (in cyan). (B) Superposition of compound-22A against $A_{2A}AR$ (in compound-22A binding mode) at the beginning (in yellow) and last MD trajectory (in cyan). (C) Superposition of compound-22B against $A_{2A}AR$ at the beginning (in yellow) and last MD trajectory (in cyan). The protein is shown as a white cartoon. The hydrogen bonds between compound 22 and ARs are represented by dashed lines. The side chains of Phe171^{ECL2} and Asn254$^{6.55}$ (Tyr9$^{1.35}$, Ser67$^{2.65}$, Phe168^{ECL2}, Glu169^{ECL2} and Asn253$^{6.55}$ in $A_{2A}AR$) are represented by sticks. The centers of the phenyl group of Phe171^{ECL2} (Phe168^{ECL2}) and the indole and pyridine rings of compound 22 are indicated by dots, and the π-tacking is represented by dashed lines. (For interpretation of the references to color in this figure legend, the reader is referred to the Web version of this article.)

Phe171^{ECL2}. The interactions were stable during the 100-ns simulation (Fig. 5A). The position of compound 22 slightly changed with an RMS$_{lig}$ value of 1.59 Å for the compound 15-A_1AR complex (Table 5). The conformation of compound 22 showed a larger change with an RMS$_{lig}$ value of 3.06 and 5.86 Å for compound-22A and compound-22B. Compound-22A moved outward to TM2 with respect to the docking pose, forming a hydrogen bond with Tyr9$^{1.35}$ and Ser67$^{2.65}$. Compound-22A lost its interactions with Phe168^{ECL2} and Asn253$^{6.55}$ with respect to the docking pose (Fig. 5B). Compound-22B showed a rotation from the docking conformation and lost the π-π stacking interaction with Phe168^{ECL2} and one hydrogen bond with Asn253$^{6.55}$ with respect to the docking pose at the end of the simulation (Fig. 5C). The calculated binding free energies for compound-22A and 22B (-32.29 and -34.00 kcal/mol) were higher than that of compound 22-A_1AR (-42.55 kcal/mol, Table S4). This result is also consistent with the experimental observation that compound 22 showed a higher binding affinity against A_1AR than against $A_{2A}AR$. This exact behavior was observed during the MD simulations of PSB36, ZM241385, and compounds 15, 20 and 22 in this study.

3. Conclusion

In this investigation, we have described the identification of antagonists with high A_1AR binding affinity by performing a multistage virtual screening of the ChemDiv library (1,492,362 compounds). Random forest, e-pharmacophore and molecular docking methods were sequentially applied in the multistage

virtual screening strategy. Among all 22 selected and tested compounds in the bioassays, 18 compounds (81.82% success) were found to exhibit substantial affinity against A_1AR in the radioligand binding assay, including six compounds with a pK$_i$ > 6. Based on the cAMP measurement results, six compounds (pK$_i$ > 6) demonstrated low micromolar antagonistic activity (pIC$_{50}$ = 5.51−6.38) against the A_1AR. In particular, four of six compounds (pK$_i$ > 6) showed good selective binding to A_1AR over $A_{2A}AR$ (>100-fold). According to the novelty analysis, four of six compounds (pK$_i$ > 6) had new scaffolds (Tc values < 0.4). Such potent modulators may be of clinical interest for the treatment of A_1AR-related human pathologies, such as Alzheimer's disease (AD), cardiac disease and kidney disease.

Molecular dynamics simulations were performed to provide insights into the selectivity of three compounds (compound 15, 20 and 22) against A_1AR over $A_{2A}AR$. According to the results, compounds 15, 20 and 22 were stabilized (RMS$_{lig}$ value ≤ 2 Å) inside the binding pocket of A_1AR with similar orientations to the docking pose in 100-ns MD simulations, whereas they escaped from the binding area of $A_{2A}AR$ with larger values of RMS$_{lig}$ (RMS$_{lig}$ ≥ 2 Å).

In brief, a multistage virtual screening strategy has been successfully used to identify relatively novel A_1AR antagonists with good binding affinity and selectivity, as verified by radioligand binding and cAMP assays. We hope that these findings provide new insights into drug discovery against A_1AR and facilitate research into new drugs and treatments for A_1AR-related human pathologies.

4. Materials and methods

4.1. Data sets

A_1AR ligands with annotated activity values were downloaded from the ChEMBL database [57]. To investigate the effect of activity cutoffs in training data on the performance of machine learning models, we constructed three datasets, namely, K-200, K-1000 and K-2000. The K-200 contains 1112 known active molecules at A_1AR ($K_i < 100$ nM) and 1998 inactive molecules at A_1AR ($K_i > 200$ nM). The K-1000 comprises 1112 known active molecules at A_1AR ($K_i < 100$ nM) and 997 inactive molecules at A_1AR ($K_i > 1000$ nM). The K-2000 includes 449 active molecules at A_1AR ($K_i < 20$ nM) and 623 inactive molecules at A_1AR ($K_i > 2000$ nM). Each dataset was divided into a training set (80% of the dataset) and a test set (20% of the dataset) using the stratified sampling method.

In addition, a validation data set consisting of 37 known A_1AR antagonists ($K_i < 20$ nM) and 1332 decoys (36 decoys of each active molecule) was used to evaluate the performance of the e-pharmacophore model. With respect to known antagonists, decoys were selected from the ZINC database [58,59] using DecoyFinder2.0 [60] based on the principles of a Tanimoto coefficient < 0.75, molecular weight $\pm$ 25, hydrogen bond acceptors $\pm$ 2, hydrogen bond donors $\pm$ 1 and logP $\pm$ 1, while a Tanimoto coefficient < 0.9 was used with respect to other decoys.

The compounds in the training set, test set, validation set and ChemDiv database were prepared using the LigPrep [61] module of the Schrödinger 2017 molecular modeling package to add hydrogen atoms, convert 2D structures to 3D, generate stereoisomers and determine the ionization state at pH 7.0 ± 2.0 with Epik [62]. Energy minimized 3D structures were obtained using an OPLS_2005 force field. ConfGen [63] with default parameters was utilized to generate conformers for the compounds in the validation set and ChemDiv database, which were used for pharmacophore screening.

4.2. Random forest modeling

In this study, the RF algorithm developed by Breiman was used to construct classifiers [64]. The molecular descriptors of the compounds in the K-200, K-1000 and K-2000 sets were initially calculated with Dragon6.0 [65], which were used as input data to generate the RF models using the "RandomForest" package implemented in the KNIME program [49]. The training parameters of "Number of models" and "Use static random seed" were set to 600 and 20181217, respectively. The other parameters employed default values. The best performance of the RF model was further utilized to screen the ChemDiv database.

4.3. E-pharmacophore model

The e-Pharmacophore modeling has the advantages of both ligand- and structure-based approaches by generating energetic optimization. The e-Pharmacophore hypothesis in this study was generated using the PHASE module of Schrödinger 2017 [66]. The crystal structure (PDB ID 5N2S) of the A_1AR in complex with an antagonist, which was resolved by Cheng et al., in 2017 [10], was extracted from the RCSB Protein Data Bank (PDB) and used to build the e-pharmacophore model. The protein structure was then prepared using the Protein Preparation Wizard module [67] in Schrödinger 2017 to remove all crystallographic water molecules, correct side chains with missing atoms, add hydrogen atoms and assign protonation states and partial charges with the OPLS_2005 force field for the e-Pharmacophore model and docking studies. Finally, the crystal structure was minimized until the root-mean-square deviation (RMSD) of the nonhydrogen atoms reached ≤ 0.3 Å.

Prior to generating the e-pharmacophore hypothesis, PSB36 (cocrystallized selective A_1AR antagonist) was initially extracted from the cocrystallized PDB complex (PDB ID 5N2S) and then redocked back to the A_1AR crystal structure using Glide XP precision mode with the "Refine" option to accurately characterize the protein-ligand interactions. Default settings were employed for the refinement and scoring. The e-pharmacophore hypothesis was automatically generated based on six chemical features, namely, hydrogen-bond acceptor (A), hydrogen-bond donor (D), hydrophobe (H), negative ionizable (N), positive ionizable (P) and aromatic ring (R). The process of quantification and sorting of each pharmacophore feature site was performed as previously described [51].

4.4. Molecular docking

All molecular docking studies were performed using the Virtual Screening Workflow [68]. The cocrystal structure (PDB ID 5N2S) was used to build the energy grid, which was generated at the centroid of the cocrystallized ligand. The protocol constraints including QikProp and Lipinski filters were employed to filter compounds with suitable pharmacological properties. Glide HTVS, SP and XP score functions were used to estimate the binding affinity of receptor ligands and to rank them according to their predicted scores. The top 50% good scoring compounds through HTVS docking were filtered using SP. The top 50% good scoring compounds through SP docking were filtered using XP. The top 25% good scoring compounds through XP were further processed using Prime MM-GBSA postprocessing. All other parameters used in the grid generation and docking utilized default settings.

4.5. Adenosine binding assays

In vitro radioligand binding competition assays were carried out using the human A_1 and A_{2A} ARs expressed in transfected CHO cells. All 22 tested compounds were purchased from J&K Scientific Ltd. (Shanghai, China). Pharmaron (Beijing) was commissioned to perform the in vitro adenosine binding assays. All compounds were dissolved (20 mM) in dimethyl sulfoxide (DMSO) and further diluted using DMSO. The final concentrations of the test compounds in the reaction system ranged from 5.08×10^{-3} to 100 μM with ten 3-fold dilution concentrations, with a final concentration of DMSO less than 1%.

4.5.1. Human A_1 adenosine receptor

For the A_1AR assay, all 22 compounds (No. 1–22) were tested in radioligand binding assays at the human A_1AR ([^{3}H]DPCPX), and [^{3}H]DPCPX was used as the radioligand. The DPCPX served as a positive control. Competition binding experiments of [^{3}H]DPCPX (2.5 nM) against A_1AR (4 μg/well) and ten different concentrations of compounds were performed for 50 min at 25 °C in 50 μL of assay buffer (50 mM Tris-HCl, 10 mM $MgCl_2$, 1 mM EDTA, 1 μg/ml adenosine deaminase, pH 7.4).

4.5.2. Human A_{2A} adenosine receptor

For the $A_{2A}AR$ assay, the compounds were tested in radioligand binding assays against human $A_{2A}AR$ ([^{3}H]ZM241385), and ([^{3}H]ZM241385) was used as the radioligand. The 4-[2-[[7-amino-2-(furyl)1,2,4-triazolo[2,3-a]1,3,5-triazin-5-yl]-amino]ethyl]phenol (ZM241385) served as the positive control. Displacement experiments of [^{3}H]ZM241385 (0.5 nM) to $A_{2A}AR$ (9 μg/well) were performed in 500 μL of assay buffer (50 mM Tris-HCl, 10 mM $MgCl_2$, 1 mM EDTA, 1 μg/ml adenosine deaminase, pH 7.4) and ten different concentrations of compounds for 90 min at 27 °C.

4.5.3. Data analysis

For compounds that inhibited radioligand binding at A_1AR and $A_{2A}AR$ by more than 50% at the top concentration (100 μM), IC_{50} values were determined from the sigmoidal concentration-response curves, which were generated using Xlfit (Version 5.3.1; IDBS, Guildford, UK) by plotting the counts per minute (CPM) against the logarithm of the ligand concentrations. K_i values for antagonists were calculated based on the IC_{50} values using the Cheng-Prusoff equation $K_i = IC_{50}/(1 + [C^*]/K_d^*)$, where $[C^*]$ and K_d^* is the concentration of the radioligand and the equilibrium dissociation constant for the radioligand, respectively [69]. For A_1AR binding, the $[C^*]$ and K_d^* of the radioligand [3H]DPCPX were 2.5 nM and 2.1 nM, respectively. For $A_{2A}AR$ binding, the $[C^*]$ and K_d^* of the radioligand [3H]ZM241385 were 0.5 nM and 2.06 nM, respectively. The K_d determination curves of [3H]DPCPX and [3H]ZM241385 are shown in Fig. S8.

4.6. A_1 adenosine receptor functional assay

The test compounds were evaluated as A_1AR antagonists by A_1AR-mediated cAMP production in a cell-based functional assay. CHO-A_1 cells, CHO-K1 cells that are engineered to express the human A_1AR, were cultured in growth medium (Ham's F12K + 10% FBS + 1*Ps + 800 μg/ml Hygromycin B (HB)) at 37 °C and 5% CO_2. The cells were collected by centrifugation and resuspended in Hank's Balanced Salt Solution (HBSS), 0.1% bovine serum albumin (BSA), 20 mM N-(2-hydroxyethyl)- piperazine-N′-ethanesulfonic acid (HEPES) and 100 nM 3- isobutyl-1-methylxanthine (IBMX). Next, 8000 cells/well were added to a 384-well assay plate. The test compounds were prepared in DMSO as 3-fold dilutions of 10 concentrations. The antagonist activity of the test compounds was evaluated by assessing their ability to counteract the agonist (5′-N-ethylcarboxamidoadenosine, NECA)-mediated decrease in cAMP accumulation. The forskolin (8 μM) and NECA (40 nM) mixture was added to the cell plate and incubated at 37 °C for 30 min Eu^{3+} cryptate-labeled anti-cAMP antibody (10 μl) and d2-labeled cAMP (10 μl) were added to the cell plate and incubated at room temperature for 1 h. The fluorescence signal was measured at 665 nm and 615 nm using an Envision 2104 plate reader.

4.7. Molecular dynamics simulation

The molecular docking study was performed with Maestro 10.1 in the Schrödinger program [70]. We prepared A_1 and A_{2A} ARs proteins for the docking calculation. Here, the X-ray crystallographic structure of the antagonist PSB36 bound to the A_1AR thermostable mutant (PDB ID 5N2S) [9] and PSB36 bound to the $A_{2A}AR$-StaR2 mutant (PDB ID 5N2R) [9] were subsequently selected and prepared for the docking analysis and MD simulation. Both the antagonist PSB36-bound A_1AR thermostable mutant and PSB36-bound $A_{2A}AR$-StaR2 mutant contained nine mutations (5N2S: $A54L^{2.52}$, $T88A^{3.36}$, $R107A^{3.55}$, $K122A^{4.43}$, $N154A^{ECL2}$, $L202A^{5.63}$, $L235A^{6.37}$, $V239A^{6.41}$, and $S277A^{7.42}$, and 5N2R: $A54L^{2.52}$, $T88A^{3.36}$, $R107A^{3.55}$, $K122A^{4.43}$, $N154A^{ECL2}$, $L202A^{5.63}$, $L235A^{6.37}$, $V239A^{6.41}$, and $S277A^{7.42}$). The thermostabilizing mutations were mutated back to the wild type and T4 lysozyme, and unnecessary small molecules were separately removed from the crystal structures. The missing residues were constructed by homology modeling using the Prime module of Schrödinger [71]. The Protein Preparation Wizard module of Schrödinger [67] was applied to add hydrogen. The protonation states for the hydroxyl, Asn, Gln, and His were optimized using the ProtAssign module of Schrödinger [67].

Prior to the docking calculations, PSB36 was used to extract the A_1AR and $A_{2A}AR$ crystal structure, which were then docked into the original binding pocket of their own receptor. The results revealed approximately the same binding mode in the X-ray crystallographic structure. Thus, compounds 15, 20 and 22 were docked into the same site of A_1AR and $A_{2A}AR$. During the docking process, the ChemScore empirical scoring function [72] was applied to the conformational search for the protein-ligand binding structure. Among a series of docking parameters, the grid size was set to be similar to the PSB36. The pose with the lowest free energy of binding was selected as the best binding mode. Docking poses for each ligand were visualized using maestro [70]. Compound 15 provided a similar docking pose against A_1 and A_{2A} ARs, excluding compounds 20 and 22. Compounds 20 and 22 showed different orientations (we denote binding mode A) for binding with A_1 and A_{2A} ARs. Thus, we performed the second round of docking using the core pattern comparison method. We used the pose of compounds 20 and 22 against A_1AR as reference poses and restricted docking to the position with a tolerance value of 2 Å. The results showed the orientation for compounds 20 and 22 (binding mode B) in similar docking poses against A_1AR.

Thus, MD simulations were performed to investigate the basic binding mode features for compounds exhibiting selective affinity to A_1 and A_{2A} ARs. The ten complexes with the determined docking poses were subsequently prepared for MD simulation. Each of the complex structure was inserted into 95 Å × 80 Å POPE bilayers, with the TIP3P water solvated and 0.15 M NaCl neutralized. Each system included approximately 71,500 atoms. The dimensions of each system were 95 Å × 80 Å × 110 Å.

The molecular dynamic simulations were carried out using the PMEMD module of AMBER18 [73]. The AMBER FF14SB force field [74] was used for A_1 and A_{2A} ARs. By using the LEAP plugin in AMBER 18 [73], the protein residues were set to standard protonation states at appropriate protonation states, calculated using the H++ program [75]. We generated prmtop and inpcrd files for PSB36 and compounds 15, 20 and 22 using the general force field [76] (GAFF) with Antechamber in AMBER 18 [73]. The AMBER lipid force field LIPID14 [77] was used for POPE. The time step was set to 2 fs for all simulations. We performed the minimization, thermalization and equilibration for all nine systems. First, each system was minimized for 10000 steps. Second, thermalization of the heating for each system from 0 K to 310 K was carried out in 500 ps using the Langevin [78] thermostat, followed by equilibration for 5 ns using NVT ensemble. The protein, ligand and lipid head groups were fixed with the constraint of 50 kcal mol^{-1} Å^{-2}. Third, the systems were equilibrated for 30 ns using the NPT ensemble, and A_1AR and NECA were constrained with the position restraints, which were gradually reduced from 50 (20 ns) to 10 (5 ns) and 2 kcal mol^{-1} Å^{-2} (5 ns). Finally, the 100-ns cMD simulation for each system was performed under a constant pressure (NPT) with no constraints. A 12 Å cut-off was set for the nonbonded interaction. The SHAKE [79] algorithm integration was used to constrain covalent bonds involving hydrogen atoms, and the particle mesh Ewald (PME) [80] algorithm was applied to treat Long-range electrostatic interactions. The frames were saved every 5000 steps for analysis.

The trajectory was analyzed with the VMD [81] and CPPTRAJ tools in AMBER18 [73]. Binding free energies between the compounds and protein molecules were calculated with the MM-PBSA module in Amber18, and the Poisson−Boltzmann surface area (MM-PBSA) method [82] was used.

Declaration of competing interest

The authors declare that they have no known competing financial interests or personal relationships that could have appeared to influence the work reported in this paper.

Acknowledgments

Appendix A. Supplementary data

Supplementary data to this article can be found online at https://doi.org/10.1016/j.ejmech.2019.111936.

References

[1] M. Rekik, S.J. Mustafa, Adenosine receptors, J. Biol. Chem. 267 (2002) 6451–6454.

[2] T.M. Palmer, G.L. Stiles, Adenosine receptors, Neuropharmacology 34 (1995) 683–694.

[3] B.B. Fredholm, A.P. IJzerman, K.A. Jacobson, K.N. Klotz, J. Linden, International Union of Pharmacology. XXV. Nomenclature and classification of adenosine receptors, Pharmacol. Rev. 53 (2001) 527–552.

[4] J.F. Chen, H.K. Eltzschig, B.B. Fredholm, Adenosine receptors as drug targets-what are the challenges? Nat. Rev. Drug Discov. 12 (2013) 265–286.

[5] K.A. Jacobson, Z.-G. Gao, Adenosine receptors as therapeutic targets, Nat. Rev. Drug Discov. 5 (2006) 247–264.

[6] I. Feoktistov, I. Biaggioni, R. Polosa, S.T. Holgate, Adenosine A(2B) receptors: a novel therapeutic target in asthma? Trends Pharmacol. Sci. 19 (1998) 148–153.

[7] S.A. Poulsen, R.J. Quinn, Adenosine receptors: new opportunities for future drugs, Bioorg. Med. Chem. 6 (1998) 619–641.

[8] H. Gutiérrez-De-Terán, J. Sallander, E. Sotelo, Structure-based rational design of adenosine receptor ligands, Curr. Top. Med. Chem. 17 (2017) 40–58.

[9] A. Glukhova, D.M. Thal, A.T. Nguyen, E.A. Vecchio, M. Jörg, P.J. Scammells, L.T. May, P.M. Sexton, A. Christopoulos, Structure of the adenosine A1 receptor reveals the basis for subtype selectivity, Cell 168 (2017) 867–877.

[10] R.K.Y. Cheng, E. Segala, N. Robertson, F. Deflorian, A.S. Doré, J.C. Errey, C. Fiez-Vandal, F.H. Marshall, R.M. Cooke, Structures of human A1and A2A adenosine receptors with xanthines reveal determinants of selectivity, Structure 25 (2017) 1275–1285.

[11] P. Lagarias, E. Vrontaki, G. Lambrinidis, D. Stamatis, M. Convertino, G. Ortore, T. Mavromoustakos, K.N. Klotz, A. Kolocouris, Discovery of novel adenosine receptor antagonists through a combined structure- and ligand-based approach followed by molecular dynamics investigation of ligand binding mode, J. Chem. Inf. Model. 58 (2018) 794–815.

[12] J. Kim, J. Wess, A.M. van Rhee, T. Schöneberg, K.A. Jacobson, Site-directed mutagenesis identifies residues involved in ligand recognition in the human A 2a adenosine receptor, J. Biol. Chem. 270 (1995) 13987–13997.

[13] D. van Calker, M. Müller, B. Hamprecht, Adenosine regulates via two different types of receptors, the accumulation of cyclic amp in cultured brain cells, J. Neurochem. 33 (1979) 999–1005.

[14] F. Libert, S.N. Schiffmann, A. Lefort, M. Parmentier, C. Gérard, J.E. Dumont, J.J. Vanderhaeghen, G. Vassart, The orphan receptor cDNA RDC7 encodes an A1 adenosine receptor, EMBO J. 10 (2018) 1677–1682.

[15] C.E. Müller, A1-Adenosine receptor antagonists, Expert Opin. Ther. Pat. 7 (1997) 419–440.

[16] B. Hocher, Adenosine A1 receptor antagonists in clinical research and development, Kidney Int. 78 (2010) 438–445.

[17] M.J. Lohse, K.N. Klotz, J. Lindenborn-Fotinos, M. Reddington, U. Schwabe, R.A. Olsson, 8-Cyclopentyl-1,3-dipropylxanthine (DPCPX) - a selective high affinity antagonist radioligand for A1 adenosine receptors, Naunyn. Schmiedebergs. Arch. Pharmacol. 336 (1987) 204–210.

[18] A.S. Robeva, R.L. Woodard, X. Jin, Z. Gao, S. Bhattacharya, H.E. Taylor, D.L. Rosin, J. Linden, Molecular characterization of recombinant human adenosine receptors, Drug Dev. Res. 39 (1996) 243–252.

[19] B.M. Massie, C.M. O'Connor, M. Metra, P. Ponikowski, J.R. Teerlink, G. Cotter, B.D. Weatherley, J.G.F. Cleland, M.M. Givertz, A. Voors, P. DeLucca, G.A. Mansoor, C.M. Salerno, D.M. Bloomfield, H.C. Dittrich, Rolofylline, an adenosine A 1 –Receptor antagonist, in acute heart failure, N. Engl. J. Med. 363 (2010) 1419–1428.

[20] J.R. Teerlink, V.J. Iragui, J.P. Mohr, P.E. Carson, P.J. Hauptman, D.H. Lovett, A.B. Miller, I.L. Piña, S. Thomson, P.D. Varosy, M.R. Zile, J.G.F. Cleland, M.M. Givertz, M. Metra, P. Ponikowski, A.A. Voors, B.A. Davison, G. Cotter, D. Wolko, P. DeLucca, C.M. Salerno, G.A. Mansoor, H. Dittrich, C.M. O'Connor, B.M. Massie, The safety of an adenosine A1-receptor antagonist, rolofylline, in patients with acute heart failure and renal impairment: findings from PRO-TECT, Drug Saf. 35 (2012) 233–244.

[21] J. Wei, S. Wang, S. Gao, X. Dai, Q. Gao, 3D-pharmacophore models for selective A2A and A2B adenosine receptor antagonists, J. Chem. Inf. Model. 47 (2007) 613–625.

[22] E. Van Der Horst, P. Marqués-Gallego, T. Mulder-Krieger, J. Van Veldhoven, J. Kruisselbrink, A. Aleman, M.T.M. Emmerich, J. Brussee, A. Bender, A.P. Ijzerman, Multi-objective evolutionary design of adenosine receptor ligands, J. Chem. Inf. Model. 52 (2012) 1713–1721.

[23] M. Bacilieri, A. Ciancetta, S. Paoletta, S. Federico, S. Cosconati, B. Cacciari, S. Taliani, F. Da Settimo, E. Novellino, K.N. Klotz, G. Spalluto, S. Moro, Revisiting a receptor-based pharmacophore hypothesis for human A 2A adenosine receptor antagonists, J. Chem. Inf. Model. 53 (2013) 1620–1637.

[24] F. Sirci, L. Goracci, D. Rodríguez, J. van Muijlwijk-Koezen, H. Gutiérrez-de-Terán, R. Mannhold, Ligand-, structure- and pharmacophore-based molecular fingerprints: a case study on adenosine A(1), A (2A), A (2B), and A (3) receptor antagonists, J. Comput. Aided Mol. Des. 26 (2012) 1247–1266.

[25] I. Bonet, P. Franco-Montero, V. Rivero, M. Teijeira, F. Borges, E. Uriarte, A. Morales Helguera, Classifier ensemble based on feature selection and diversity measures for predicting the affinity of A2B adenosine receptor antagonists, J. Chem. Inf. Model. 53 (2013) 3140–3155.

[26] S. El-Taher, K.M. El-Sawy, R. Hilal, Electronic structure of some adenosine receptor antagonists. VQSAR investigation, J. Chem. Inf. Comput. Sci. 42 (2002) 386–392.

[27] S.K. Kim, K.A. Jacobson, Three-dimensional quantitative structure - activity relationship of nucleosides acting at the A3 adenosine receptor: analysis of binding and relative efficacy, J. Chem. Inf. Model. 47 (2007) 1225–1233.

[28] L. Miclielan, F. Stephanie, L. Terfloth, D. Hristozov, B. Cacciari, K.N. Klotz, G. Spalluto, J. Gasteiger, S. Moro, Exploring potency and selectivity receptor antagonist profiles using a multilabel classification approach: the human adenosine receptors as a key study, J. Chem. Inf. Model. 49 (2009) 2820–2836.

[29] S. Tian, X. Wang, L. Li, X. Zhang, Y. Li, F. Zhu, T. Hou, X. Zhen, Discovery of novel and selective adenosine A2A receptor antagonists for treating Parkinson's disease through comparative structure-based virtual screening, J. Chem. Inf. Model. 57 (2017) 1474–1487.

[30] D. Rodríguez, Z.G. Gao, S.M. Moss, K.A. Jacobson, J. Carlsson, Molecular docking screening using agonist-bound GPCR structures: probing the A2A adenosine receptor, J. Chem. Inf. Model. 55 (2015) 550–563.

[31] S. Moro, A.H. Li, K.A. Jacobson, Molecular modeling studies of human A3 adenosine antagonists: structural homology and receptor docking, J. Chem. Inf. Comput. Sci. 38 (1998) 1239–1248.

[32] V. Katritch, I. Kufareva, R. Abagyan, Structure based prediction of subtype-selectivity for adenosine receptor antagonists, Neuropharmacology 60 (2011) 108–115.

[33] C.J. Langmead, S.P. Andrews, M. Congreve, J.C. Errey, E. Hurrell, F.H. Marshall, J.S. Mason, C.M. Richardson, N. Robertson, A. Zhukov, M. Weir, Identification of novel adenosine A 2A receptor antagonists by virtual screening, J. Med. Chem. 55 (2012) 1904–1909.

[34] P. Kolb, K. Phan, Z.G. Gao, A.C. Marko, A. Sali, K.A. Jacobson, Limits of ligand selectivity from docking to models: in silico screening for A1 adenosine receptor antagonists, PLoS One 7 (2012), e49910.

[35] E. vanderHorst, R. VanderPijl, T. Mulder-Krieger, A. Bender, A.P. Ijzerman, Substructure-based virtual screening for adenosine A 2A receptor ligands, ChemMedChem 6 (2011) 2302–2311.

[36] V. Katritch, V.P. Jaakola, J.R. Lane, J. Lin, A.P. Ijzerman, M. Yeager, I. Kufareva, R.C. Stevens, R. Abagyan, Structure-based discovery of novel chemotypes for adenosine A2A receptor antagonists, J. Med. Chem. 53 (2010) 1799–1809.

[37] J. Carlsson, L. Yoo, Z.G. Gao, J.J. Irwin, B.K. Shoichet, K.A. Jacobson, Structure-based discovery of A2A adenosine receptor ligands, J. Med. Chem. 53 (2010) 3748–3755.

[38] N. Schaduangrat, N. Anuwongcharoen, C. Phanus-umporn, N. Sriwanichpoom, J.E.S. Wikberg, C. Nantasenamat, Proteochemometric Modeling for Drug Repositioning, Silico Drug Des, 2019, pp. 281–302.

[39] G.J.P. Van Westen, O.O. Van Den Hoven, R. Van Der Pijl, T. Mulder-Krieger, H. De Vries, J.K. Wegner, A.P. IJzerman, H.W.T. Van Vlijmen, A. Bender, Identifying novel adenosine receptor ligands by simultaneous proteochemometric modeling of rat and human bioactivity data, J. Med. Chem. 55 (2012) 7010–7020.

[40] M.N. Drwal, R. Griffith, Combination of ligand- and structure-based methods in virtual screening, Drug Discov. Today Technol. 10 (2013) e395–e401.

[41] M. Miteva, Hierarchical structure-based virtual screening for drug design, Biotechnol. Biotechnol. Equip. 22 (2008) 634–638.

[42] P. Mistry, D. Neagu, P.R. Trundle, J.D. Vessey, Using random forest and decision tree models for a new vehicle prediction approach in computational toxicology, Soft Comput 20 (2016) 2967–2979.

[43] H. Singh, S. Singh, D. Singla, S.M. Agarwal, G.P.S. Raghava, QSAR based model for discriminating EGFR inhibitors and non-inhibitors using Random forest, Biol. Direct 10 (2015) 10.

[44] P. Kumari, A. Nath, R. Chaube, Identification of human drug targets using machine-learning algorithms, Comput. Biol. Med. 56 (2015) 175–181.

[45] D. Zilian, C.A. Sotriffer, SFCscoreRF, A random forest-based scoring function for improved affinity prediction of protein-ligand complexes, J. Chem. Inf. Model. 53 (2013) 1923–1933.

[46] V. Svetnik, A. Liaw, C. Tong, J. Christopher Culberson, R.P. Sheridan, B.P. Feuston, Random forest: a classification and regression tool for compound classification and QSAR modeling, J. Chem. Inf. Comput. Sci. 43 (2003) 1947–1958.

[47] D. Ruano-Ordás, I. Yevseyeva, V.B. Fernandes, J.R. Méndez, M.T.M. Emmerich, Improving the drug discovery process by using multiple classifier systems, Expert Syst. Appl. 121 (2019) 292–303.

[48] M. Luo, X.S. Wang, B.L. Roth, A. Golbraikh, A. Tropsha, Application of quantitative structure-activity relationship models of 5-HT1A receptor binding to virtual screening identifies novel and potent 5-HT1A ligands, J. Chem. Inf.

Model. 54 (2014) 634—647.

[49] M.R. Berthold, N. Cebron, F. Dill, T.R. Gabriel, T. Kötter, T. Meinl, P. Ohl, K. Thiel, B. Wiswedel, KNIME - the Konstanz information miner, ACM SIGKDD Explor, Newsletter 11 (2009) 26—31.

[50] J.-F. Truchon, C.I. Bayly, Evaluating virtual screening methods: good and bad metrics for the "early recognition" problem, J. Chem. Inf. Model. 47 (2007) 488—508.

[51] Y. Wei, J. Li, J. Qing, M. Huang, M. Wu, F. Gao, D. Li, Z. Hong, L. Kong, W. Huang, J. Lin, Discovery of novel hepatitis C virus NS5B polymerase inhibitors by combining random forest, multiple e-pharmacophore modeling and docking, PLoS One 11 (2016), e0148181.

[52] Canvas, Schrödinger, LLC, New York, NY, 2017.

[53] D. Rogers, M. Hahn, Extended-connectivity fingerprints, J. Chem. Inf. Model. 50 (2010) 742—754.

[54] R. Link, J.K. von Frijtag Drabbe Künzel, A. Göblyös, A.P. IJzerman, M. Mantri, J. van Veldhoven, T. Mulder-Krieger, M.W. Beukers, H. de Vries, O. de Graaf, J. Brussee, 2-Amino-6-furan-2-yl-4-substituted nicotinonitriles as A 2A adenosine receptor antagonists, J. Med. Chem. 51 (2008) 4449—4455.

[55] K.N. Klotz, Adenosine receptors and their ligands, Naunyn. Schmiedebergs. Arch. Pharmacol. 362 (2000) 382—391.

[56] S. Moro, Z.G. Gao, K.A. Jacobson, G. Spalluto, Progress in the pursuit of therapeutic adenosine receptor antagonists, Med. Res. Rev. 26 (2006) 131—159.

[57] A. Gaulton, A. Hersey, M.L. Nowotka, A. Patricia Bento, J. Chambers, D. Mendez, P. Mutowo, F. Atkinson, L.J. Bellis, E. Cibrian-Uhalte, M. Davies, N. Dedman, A. Karlsson, M.P. Magarinos, J.P. Overington, G. Papadatos, I. Smit, A.R. Leach, The ChEMBL database in 2017, Nucleic Acids Res. 45 (2017) D945—D954.

[58] J.J. Irwin, B.K. Shoichet, Zinc — a free database of commercially available compounds for virtual screening supporting information, J. Chem. Inf. Model. 45 (2005) 177—182.

[59] J.J. Irwin, T. Sterling, M.M. Mysinger, E.S. Bolstad, R.G. Coleman, ZINC: a free tool to discover chemistry for biology, J. Chem. Inf. Model. 52 (2012) 1757—1768.

[60] A. Cereto-Massagué, L. Guasch, C. Valls, M. Mulero, G. Pujadas, S. Garcia-Vallvé, DecoyFinder: an easy-to-use python GUI application for building target-specific decoy sets, Bioinformatics 28 (2012) 1661—1662.

[61] LigPrep, Schrödinger, LLC, New York, NY, 2017.

[62] Epik, Schrödinger, LLC, New York, NY, 2017.

[63] ConfGen, Schrodinger, LLC, New York, NY, 2017.

[64] L. BREIMAN, Random forests, Mach. Learn. 45 (2001) 5—32.

[65] DRAGON, Version 6.0; Talete Srl: Milano, Italy, 2011.

[66] Phase, Schrödinger, LLC, New York, NY, 2017.

[67] Schrödinger Suite 2017 Protein Preparation Wizard; Epik, Schrödinger, LLC, New York, NY, 2017. Impact, Schrödinger, LLC, New York, NY, 2017; Prime, Schrödinger, LLC, New York, NY, 2017.

[68] Schrödinger Suite, Virtual Screening Workflow, LLC, New York, NY, 2017.

[69] C. Yung-Chi, W.H. Prusoff, Relationship between the inhibition constant (KI) and the concentration of inhibitor which causes 50 per cent inhibition (I50) of an enzymatic reaction, Biochem. Pharmacol. 22 (1973) 3099—3108.

[70] Maestro, Schrödinger, L.L.C., New York, NY, 2017.

[71] Prime, Schrödinger, LLC, New York, NY, 2017.

[72] M.D. Eldrige, C.W. Murray, T.R. Auton, G. V Paolini, R.P. Mee, Empirical scoring functions: I. The development of a fast empirical scoring function to estimate the binding affinity of ligands in receptor complexes, J. Comput. Aided Mol. Des. 11 (1997) 425—445.

[73] D.A. Case, I.Y. Ben-Shalom, S.R. Brozell, D.S. Cerutti, T.E. Cheatham III, V.W.D. Cruzeiro, T.A. Darden, R.E. Duke, D. Ghoreishi, M.K. Gilson, H. Gohlke, A.W. Goetz, D. Greene, R. Harris, N. Homeyer, S. Izadi, A. Kovalenko, T. Kurtzman, T.S. Lee, S. LeGrand, P. Li, C. Lin, J. Liu, T. Luchko, R. Luo, D.J. Mermelstein, K.M. Merz, Y. Miao, G. Monard, C. Nguyen, H. Nguyen, I. Omelyan, A. Onufriev, F. Pan, R. Qi, D.R. Roe, A. Roitberg, C. Sagui, S. Schott-Verdugo, J. Shen, C.L. Simmerling, J. Smith, R. Salomon-Ferrer, J. Swails, R.C. Walker, J. Wang, H. Wei, R.M. Wolf, X. Wu, L. Xiao, D.M. York, P.A. Kollman, AMBER 2018, Univ. California, San Fr, 2018.

[74] J.A. Maier, C. Martinez, K. Kasavajhala, L. Wickstrom, K.E. Hauser, C. Simmerling, ff14SB: improving the accuracy of protein side chain and backbone parameters from ff99SB, J. Chem. Theory Comput. 11 (2015) 3696—3713.

[75] R. Anandakrishnan, B. Aguilar, A. V Onufriev, H++3.0: automating pK prediction and the preparation of biomolecular structures for atomistic molecular modeling and simulations, Nucleic Acids Res. 40 (2012) W537—W541.

[76] J. Wang, R.M. Wolf, J.W. Caldwell, P.A. Kollman, D.A. Case, Development and testing of a general amber force field, J. Comput. Chem. 25 (2004) 1157—1174.

[77] C.J. Dickson, B.D. Madej, A.A. Skjevik, R.M. Betz, K. Teigen, I.R. Gould, R.C. Walker, Lipid14: the amber lipid force field, J. Chem. Theory Comput. 10 (2014) 865—879.

[78] R.W. Pastor, B.R. Brooks, A. Szabo, An analysis of the accuracy of Langevin and molecular dynamics algorithms, Mol. Phys. 65 (1988) 1409—1419.

[79] J.-P. Ryckaert, G. Ciccotti, H.J.C. Berendsen, Numerical integration of the cartesian equations of motion of a system with constraints: molecular dynamics of N-alkanes, J. Comput. Phys. 23 (1977) 327—341.

[80] T. Darden, D. York, L. Pedersen, Particle mesh Ewald: an N -log(N) method for Ewald sums in large systems, J. Chem. Phys. 98 (1993) 10089—10092.

[81] W. Humphrey, A. Dalke, K. Schulten, VMD: visual molecular dynamics, J. Mol. Graph. Model. 14 (1996) 33—38.

[82] B. Kuhn, P. Gerber, T. Schulz-Gasch, M. Stahl, Validation and use of the MM-PBSA approach for drug discovery, J. Med. Chem. 48 (2005) 4040—4048.